CHEMISTRY OF MATERIALS

pubs.acs.org/cm Article

Native Defect Engineering in $CuInTe_2$

Jesse M. Adamczyk,*,‖ Lídia C. Gomes,*,‖ Jiaxing Qu, Grace A. Rome, Samantha M. Baumann, Elif Ertekin, and Eric S. Toberer

Cite This: *Chem. Mater.* 2021, 33, 359−369 Read Online

ACCESS | Metrics & More | Article Recommendations | Supporting Information

ABSTRACT: Ternary diamond-like semiconductors, such as $CuInTe_2$, are known to exhibit promising p-type thermoelectric performance. However, the interplay between growth conditions, native defects, and thermoelectric properties have limited their realization. First-principles calculations of $CuInTe_2$ indicate that the electronic properties are controlled by three dominant defects: V_{Cu}, Cu_{In}, and In_{Cu}. The combination of these low-energy defects with significant elemental chemical potential phase space for $CuInTe_2$ yields a broad phase width. To validate these calculations, polycrystalline, bulk samples were prepared and characterized for their structural and thermoelectric properties as a function of stoichiometry. Collectively, the off-stoichiometric samples show a range of carrier concentrations that span 5 orders of magnitude (10^{15} to 10^{19} h^+ cm^{-3}). Mobility of the off-stoichiometric samples suggests that copper vacancies act as strongly scattering point-defect sites, while the other native defects scatter less strongly. Such vacancy scattering extends to the thermal conductivity where a reduction in κ_L is observed and contributes to enhanced thermoelectric performance. Understanding and controlling the native defects in $CuInTe_2$ provides a route toward n-type dopability as well as rational optimization of the p-type material.

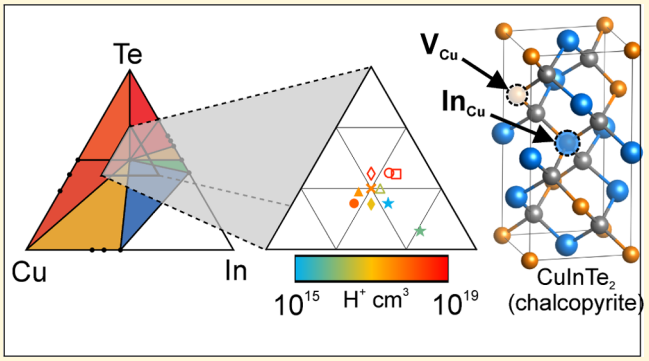

INTRODUCTION

Ternary diamond-like semiconductors (DLS) are a broad class of electronic materials that have recently emerged for thermoelectric applications. Such materials upend a long-held presumption that tetrahedrally bonded materials would have significant thermal conductivity. Instead, these materials have been found to show simultaneously high mobility and low thermal conductivity—a desirable combination for thermoelectric performance. However, the chemical complexity of these ternaries presents challenges, some of which are familiar to the optoelectronics community. In particular, native defects can profoundly affect the dopability and transport properties of such materials; furthermore, these defects are highly sensitive to growth conditions. In this work, we undertake an in-depth study of the native defects in the thermoelectric material $CuInTe_2$ to provide defect engineering strategies.

The use of DLS materials in thermoelectrics dates back to the 1970s when diamond-structure Si−Ge solid solutions were used for power generation on deep space probes (Voyager 1 through New Horizons). The high operating temperature (~1200 K) and low conversion efficiency of Si−Ge solid solutions have limited their use to highly specialized applications. Over the same time period during which Si−Ge was being used, diamond-like materials with zinc-blend and chalcopyrite structures (Figure 1a) were being developed for photovoltaic and optoelectronic applications. The chalcopyrite-type material $Cu(In,Ga)Se_2$ (CIGS) has been extensively

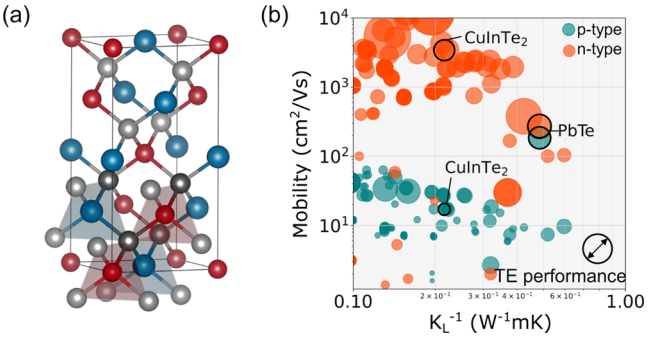

Figure 1. (a) $CuInTe_2$ in chalcopyrite-type structure with tetrahedrally bonded cation and anion atoms. Red, blue, and gray atoms stand for copper, indium, and tellurium atoms, respectively. (b) Computationally modeled transport properties for electrons and holes in DLSs. The marker size scales with the semi-empirical thermoelectric quality factor β_{SE}.[30]

Received: October 15, 2020
Revised: December 7, 2020
Published: December 16, 2020

https://dx.doi.org/10.1021/acs.chemmater.0c04041
Chem. Mater. 2021, 33, 359−369

studied for use in photovoltaics, while zinc-blende-type ZnSe has found use in LEDs and scintillators.[1−6] CIGS's low values of carrier concentration (~10^{16} cm^{-3}) and mobility (~10 cm^2/V·s) along with the high thermal conductivity of ZnSe has prevented significant efforts to improve thermoelectric performance.[7−11] Prior to the 2000s, DLS materials were largely discounted for use in thermoelectrics; however, over the last decade, various DLSs have emerged as candidates for high thermoelectric performance[12−15]

In 2012, the I−III-Te_2 chalcopyrites, $CuInTe_2$ (CIT) and $CuGaTe_2$ (CGT), were identified as high-performing thermoelectric materials because of their higher carrier concentration and Seebeck coefficients.[13−16] In CIT, a peak zT value of 1.18 was found at 850 K, while CGT showed an even higher zT of 1.4 at 950 K.[13,14] Since the discovery of these high zT values, the majority of thermoelectric studies on CIT and CGT have focused on doping and microstructure engineering to increase the peak p-type performance. A number of studies has found that doping with Zn on the group III site is an effective way to increase the p-type carrier concentration.[15−21] Carr and Morelli[16] found that $CuInTe_2$ can have a minor zT improvement when doped with zinc, alloyed with $CuGaTe_2$, or both doped and alloyed simultaneously. Luo et al.[18] showed that simultaneous doping and incorporation of TiO_2 nanofibers was able to reduce the thermal conductivity by 36%. Later, similar work showed that a combination of antimony doping and ZnO nanoparticles further reduced the thermal conductivity, thereby gaining another incremental performance increase.[15]

To date, prior experimental thermoelectric work on $CuInTe_2$ has been limited to p-type compositions.[15−18,22,23] The hole carrier concentration of undoped $CuInTe_2$ can be increased by synthesizing the material with copper deficiency. It is well established that copper vacancies increase the p-type carrier concentration as the negatively charged vacancy, V_{Cu}^{-1}, acts as an electron acceptor.[24−26] Copper can only be removed from the $CuInTe_2$ lattice up to a certain amount, at which the ordered vacancy structure $CuIn_3Te_5$ forms, and the thermoelectric performance is reduced.[24,26−28] On the copper-rich side of ternary $CuInTe_2$, single crystals of copper-rich and both copper- and indium-rich samples showed higher hole carrier concentrations in comparison to the on-stoichiometric compound.[29] This is interesting because the hole carrier concentration increases when $CuInTe_2$ is made both copper-poor or copper-rich.

Calculations indicate that the n-type thermoelectric performance of $CuInTe_2$ would far surpass that of the p-type material (Figure 1b). The calculated effective mass of electrons is an order of magnitude lower than the effective mass of holes, leading to electron mobility that is orders of magnitude higher than the hole mobility.[30] Outside of thermoelectrics literature, a few reports indicate n-type behavior in $CuInTe_2$. Wasim and Albornóz[31] showed that annealing bulk $CuInTe_2$ in the presence of indium for 45 days caused n-type conductivity. It is suggested that excess indium creates an In_{Cu} defect that acts as an electron donor. Consistent with the predictions discussed above, the high mobility of the n-type $CuInTe_2$ sample (355 cm^2/V·s)[31] suggests that n-type $CuInTe_2$ could have higher thermoelectric performance than the well-known p-type material. The other reports of n-type behavior in $CuInTe_2$ utilize processing techniques that may cause non-equilibrium behavior that will be difficult to repeat in bulk samples.[32−34]

Extrinsic defects within the DLS space are sufficiently complex such that doping behavior cannot be explained by intuition. By taking a look at extrinsic defects in the sulfide and selenide chalcopyrites, insight into the complexity of extrinsic doping of $CuInTe_2$ can be gained. Extrinsic doping studies of $CuAlS_2$ indicate that group II elements (Zn, Cd, and Mg) can occupy both the Cu or Al site, thereby allowing the material to be n-type or p-type. When $CuAlSe_2$ is synthesized in a Zn-rich atmosphere, the material remains p-type; however, the carrier concentration is reduced as a result of Zn_{Cu} defects.[35] Both of these are in contrast to $CuGaTe_2$ and $CuInTe_2$ where the addition of Zn increases the hole carrier concentration. The trend suggests that Zn tends to prefer the group III site as the anion increases in size (S → Se → Te), but the role of Zn in $CuInTe_2$ is actually unclear. Studies on off-stoichiometric $CuInTe_2$ doped with zinc suggest that the defects Zn_{In}^{-}, V_{Cu}^{-}, In_{Cu}^{2+}, and Zn_{Cu}^{+} can form, but only p-type behavior is shown.[17] Addition of Zn to $CuInTe_2$ seems to increase the hole carrier concentration regardless of native stoichiometry. All other studies on the effects of extrinsic doping of $CuInTe_2$ have only identified p-type thermoelectric behavior.

In other thermoelectric materials that have limited dopability, the combination of theory and experimental defect studies has proven valuable in developing improved thermoelectric materials. In $Cu_2HgGeTe_4$, the carrier concentration was found to be only p-type as a result of V_{Cu} defects and Cu_{Hg} antisite defects. Attempts to reduce the V_{Cu} concentration through off-stoichiometric synthesis simply increased the Cu_{Hg} concentration and the p-type behavior persisted.[12] This result suggests that $Cu_2HgGeTe_4$ will be difficult to synthesize with electrons as the majority carrier. However, $Cu_2HgGeTe_4$ can be contrasted with Mg_3Sb_2, that has a similar V_{Mg} killer defect. By synthesizing Mg_3Sb_2 with an excess of Mg, the concentration of V_{Mg}^{2-} along with the corresponding hole carrier concentration is significantly reduced. This reduction in holes enabled Mg_3Sb_2 to be doped to an n-type regime. This understanding of the native defects in Mg_3Sb_2 had a two-fold effect: first, a reliable path to n-type dopability was identified, and second, the n-type Mg_3Sb_2 was found to have superior thermoelectric properties in comparison to the p-type material[36] While this Mg_3Sb_2 case is for a binary compound, it illustrates the importance of understanding native defects while showing that performance can be significantly improved before external dopants are utilized.

In this work, we consider the impact of $CuInTe_2$'s native defects on thermoelectric properties and on n-type dopability. We begin by presenting defect calculations of $CuInTe_2$ to understand how growth conditions quantitatively impact intrinsic defect concentrations. Optimal growth regimes for p-type and n-type performance are then identified. The impact of these native defects on the electronic structure is then investigated, with an eye toward perturbations of the band edge density of states. These theoretical results form the basis for an experimental campaign of synthesis and high-temperature thermoelectric property measurements. Samples were prepared with a wide variety of stoichiometries to sample the broad range of predicted native defect phenomena; the impact of these defects is seen not only in the carrier concentration but also in the electronic mobility and lattice thermal conductivity.

https://dx.doi.org/10.1021/acs.chemmater.0c04041
Chem. Mater. 2021, 33, 359−369

METHODS

Modeling and Simulations. *Defect Formation Energy and Carrier Concentrations: Overview.* Accurate and realistic descriptions of native defects in semiconductors using first-principles calculations can be performed using the standard supercell approach.[37] This method requires the evaluation of defect formation enthalpies $\Delta H(D,q)$ of defects D their relevant charge state q, which can be obtained from total energy density functional theory (DFT) calculations as[38]

$$\Delta H(D, q) = E(D, q) - E(H) - \sum_i n_i\mu_i + qE_F + E_{corr} \quad (1)$$

where $E(D,q)$ and $E(H)$ are the total energy of the defect and the host supercell, respectively. The parameter n_i accounts for the number of atoms of species i and chemical potential μ_i added ($n_i > 0$) or removed ($n_i < 0$) from the system to create the defect.

Chemical potentials describe the energy of the reservoirs with which atoms are being exchanged. For a given compound in thermodynamic equilibrium, we have $\mu_{comp} = \sum_i \mu_i$, or

$$\mu_{CuInTe_2} = \mu_{Cu} + \mu_{In} + 2\mu_{Te} \quad (2)$$

for our system of interest. If referenced to the bulk elemental phases μ_i^0, (2) can be expressed as

$$\mu_{CuInTe_2} = \{\mu_{Cu}^0 + \Delta\mu_{Cu}\} + \{\mu_{In}^0 + \Delta\mu_{In}\} + 2\{\mu_{Te}^0 + \Delta\mu_{Te}\} \quad (3)$$

with $\Delta\mu_i$ indicating the deviation of the chemical potentials from the bulk elemental phases i = Cu, In, Te. The formation enthalpy of $CuInTe_2$ $\Delta H_{CuInTe_2} = \mu_{CuInTe_2} - \mu_{Cu}^0 - \mu_{In}^0 - 2\mu_{Te}^0$ sets the limiting values of $\Delta\mu_i$ that must satisfy

$$\Delta H_{CuInTe_2} = \Delta\mu_{Cu} + \Delta\mu_{In} + 2\Delta\mu_{Te},$$
$$\Delta\mu_{Cu}, \Delta\mu_{In}, \Delta\mu_{Te} < 0 \quad (4)$$

Full stability conditions are then determined upon the consideration of competing compounds (secondary phases). For $CuInTe_2$, the competing phases are binary materials besides the elemental bulk of copper, indium, and tellurium. The range of $\Delta\mu_{Cu,In,Te}$ values at which $CuInTe_2$ is stable satisfies $\Delta H_{CuInTe_2} < \Delta H_{cc}$, with the latter the formation enthalpy of the competing compound, defined similarly as in eq 2. To obtain the stability space of $CuInTe_2$, we calculate ΔH_{cc} of the binary competing phases with structures reported in the ICSD database. The full list is presented in the Supporting Information Table 1.

Finally, the term E_{corr} estimates corrections arising from finite size effects, as elastic and electrostatic interactions between neighboring supercells. Here we use the approach proposed by Lany and Zunger[37] to account for potential alignment ($\Delta E_{pa}(D,q)$) and image charge (ΔE_i) corrections to the formation energy of the charged defects, as given by

$$\Delta E_{pa}(D, q) = q\cdot\Delta V_{pa} \quad (5)$$

$$\Delta E_i = \frac{q^2\alpha_M}{2\varepsilon\omega^{-1/3}} \quad (6)$$

where ΔV_{pa} is the potential alignment between the defect and the host calculation, α_M is the Madelung constant for the supercell geometry, ε is the dielectric constant, and ω is the supercell volume. Please refer to ref 37 for more details on the approach.

Intrinsic defect chemistry is then assessed by computing $\Delta H_{D,q}$ for all native point defects in their relevant charge states. The results are usually presented in defect diagrams, where $\Delta H(D,q)$ for all native defects are plotted as a function of the Fermi energy E_F, which varies from the valence band maximum (VBM) to the conduction band minimum (CBM). $\Delta H(D,q)$ then depends linearly on the charge state q.

The *equilibrium Fermi energy* (ε_F^{eq}) is determined by the equilibrium amongst different defects, satisfying the charge neutrality condition

$$\sum_D qC_{D,q} - n + p = 0 \quad (7)$$

In relation 7, n and p are the free electron and hole concentrations, respectively, obtained from the valence band density of states $D_V(\varepsilon)$, conduction band density of states $D_C(\varepsilon)$, and the Fermi−Dirac distribution function $f(\varepsilon)$ as

$$n = \int_{E_{CBM}}^{\infty} D_C(\varepsilon)f(\varepsilon)d\varepsilon \quad (8)$$

$$p = \int_{-\infty}^{E_{VBM}} D_V(\varepsilon)[1 - f(\varepsilon)]d\varepsilon \quad (9)$$

The defect concentration $C_{D,q}$ is obtained by

$$C_{D,q} = N\exp\left[\frac{-\Delta H(D, q)}{k_B T}\right] \quad (10)$$

where N is the concentration of the corresponding lattice sites, and k_B is the Boltzman constant. $C_{D,q}$ and ε_F^{eq} are then obtained by self-consistent solution of eqs 7−10.

DFT Calculations. The defect formation energies $\Delta H(D,q)$ were calculated from total energies of bulk and defect-containing supercells using DFT,[39,40] as implemented in the Vienna ab initio simulation package (VASP).[41] The exchange−correction energy functional was approximated by using both the generalized gradient approximation of Perdew−Burke−Ernzerhof (PBE)[42] and the Heyd-Scuseria-Ernzerhof (HSE06)[43] hybrid functional. Despite being of a higher computational cost than conventional PBE/LDA DFT calculations, hybrid functional calculations of defects often show considerable improvement in accuracy.

Core and valence electrons are treated with the projector-augmented wave formalism.[44] The Kohn−Sham orbitals were expanded using a plane-wave basis with a cutoff energy of 400 eV. Lattice parameters and atomic positions were fully relaxed until forces were lower than 1 meV/Å on each atom. For the bulk unit cells, the Brillouin zone was sampled using a Γ-centered 4 × 4 × 4 Monkhorst−Pack k-points grid.[45] For the calculations including the point defects, a 64-atom bulk (2 × 2 × 2) supercell was used with a Γ-centered 2 × 2 × 2 k-points mesh.

Total and partial density of states were computed using a finer Γ-centered grid of 30 × 30 × 28 k-points and plotted using the Sumo python toolkit.[46] Unless otherwise stated, all results are obtained using the HSE06 hybrid functional.

For the phonon dispersion of $CuInTe_2$, the supercell approach with the finite displacement method[47] was used within VASP in conjunction with the Phonopy package.[48] The atomic positions and lattice parameters were relaxed with convergence criteria of 10^{-2} meV/Å. Phonopy was used to determine the force constants, the phonon dispersions, and the phonon projected density of states using 2 × 2 × 2 supercells and a $X \times X \times X$ k-point mesh.

Spin−orbit coupling effects were evaluated in a fully relativistic plus hybrid functional calculation. Band edge positions used to plot the defect diagrams were then adjusted according to the HSE06 + SOC calculations.

Synthesis. High purity Cu (99.999%, Alpha Aesar), In (99.999%, 5N Plus), and Te (99.999%, 5N Plus) shots were weighed in batches totaling 5 g of material. Each batch of material was loaded into a clean fused silica ampoule and sealed under vacuum. Ampoules were kept as small as possible to mitigate the evaporation of elements. Ampoules were individually placed into a furnace at 900 °C for 20 min with periodic shaking at 5 min intervals. Hot ampoules were then removed from the furnace and quenched in cold water to reduce phase separation during solidification. Ingots of solidified material were removed from ampoules, ground into a powder with an agate mortar and pestle, and then sieved through a 200-mesh sieve. Approximately 3 g of powder was loaded into graphite foil-lined graphite dies. The graphite dies were loaded into a vacuum hot press. Samples were

https://dx.doi.org/10.1021/acs.chemmater.0c04041
Chem. Mater. 2021, 33, 359−369

pressed at 550 °C for 12 h under 40 MPa of pressure. The pressure on the die was released, and the die was kept at 550 °C for 1 h as an annealing treatment before cooling to room temperature. Pellets were removed from the graphite dies and hand-polished to a parallelness within ±5 μm using a final grit paper of 2000 grit.

Measurement. High-temperature measurement of the Seebeck coefficient was performed from 323 to 623 K using custom-built apparatus.[49] All samples underwent a minimum of two heating and cooling cycles during the measurement to ensure that samples were not undergoing evolution during measurement. High temperature resistivity and Hall effect measurements were performed on a custom built apparatus with a Van der Pauw geometry.[50] Thermal diffusivity measurements were performed under vacuum using a NETZSCH LFA-467 flash diffusivity system. Density was determined by the mass and geometry of the samples. Calculation of thermal conductivity was done using the Dulong-Petit approximation and the values in the Supporting Information Table S2. SEM imaging with energy-dispersive system (EDS) were performed using an FEI Quanta 600i SEM. Grain sizes of the samples were determined from 5 images at 5 different locations on each sample. For each phase in a sample, EDS measurements were taken at 5 different locations on the samples with the averaged data shown in the Supporting Information Figures S25–S38.

RESULTS AND DISCUSSION

Electronic Structure. Computation of the HSE06 electronic band structure shows that $CuInTe_2$ is a direct band gap semiconductor at Γ with band gap energy (E_g) of 0.97 eV (the PBE value is 0.20 eV). The usual parabolic dispersion observed at band extrema in semiconductors is also characteristic of this ternary telluride. The orbital decomposed band structure shows features similar to other chalcopyrite materials. The uppermost valence bands are composed mainly of Cu 3d and Te 5p antibonding orbitals, resulting in the characteristic double-degenerate heavy-hole and non-degenerate light-hole bands of tetrahedrally coordinated semiconductors. In $CuInTe_2$, these bands meet at Γ, resulting in a three-fold degenerate VBM. The bottom of the conduction band is composed mainly of In 5s and Te 5p orbitals, forming a non-degenerate parabolic band. Spin–orbit coupling effects break the triple degeneracy at Γ and the common split-off band forms (Supporting Information Figure S1).

The predicted superior performance of n-type over p-type $CuInTe_2$ is mostly due to the large difference in electron and hole density of states effective masses, m_e^* and m_h^*. Our DFT-hybrid calculations predict $m_h^* = 0.37$, while m_e^* is smaller by 1 order of magnitude: $m_e^* = 0.016$, in the units of electron mass. These values are in agreement with previous works[30] and with our experimental data, as discussed in the Native Defects section. The large difference in effective mass leads to a predicted electron mobility which is orders of magnitude higher than the hole mobility ($\mu_e = 3 \times 10^3$ and $\mu_h = 2 \times 10^1$ $cm^2\ V^{-1}\ s^{-1}$) (Figure 2).[30]

Phase Stability. The phase stability region of $CuInTe_2$, limited by the gray area in Figure 3b, spans a large portion of the chemical potential space, plotted here as a function of the chemical potentials of copper and indium. The boundaries of $\Delta\mu_i$ ($\Delta\mu_i$[poorest-i, richest-i]) for the three elemental phases i = Cu, In, and Te are $\Delta\mu_{Cu}$[−0.75, 0.00] eV, $\Delta\mu_{In}$[−1.41, −0.14] eV, and $\Delta\mu_{Te}$[−0.67, 0.00] eV. Such differences in atomic chemical potentials lead to distinct formation energies for different sets of $\Delta\mu_i$ (eq 1), resulting in largely controllable carrier concentrations.

Our first-principles calculations predict eight regions where $CuInTe_2$ forms three-phase equilibria with other compounds.

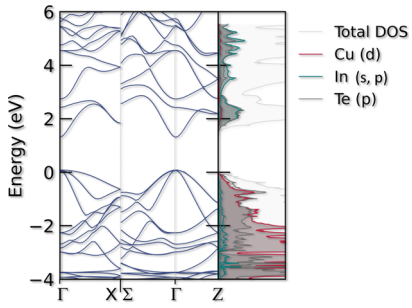

Figure 2. Electronic band structure and total and partial density of states of $CuInTe_2$ according to hybrid (HSE06) DFT calculations (the results including SOC are shown in the Supporting Information Figure S1). The usual parabolic dispersion of semiconductors with a diamond-like structure is observed here. The bottom of the conduction band is composed mainly of In 5s and Te 5p orbitals, forming a non-degenerate parabolic band. The top of the valence band is mostly formed by hybridized Cu 3d and Te 5p states, resulting in the characteristic light-hole and heavy-hole parabolic bands, triple-degenerate at Γ in $CuInTe_2$.

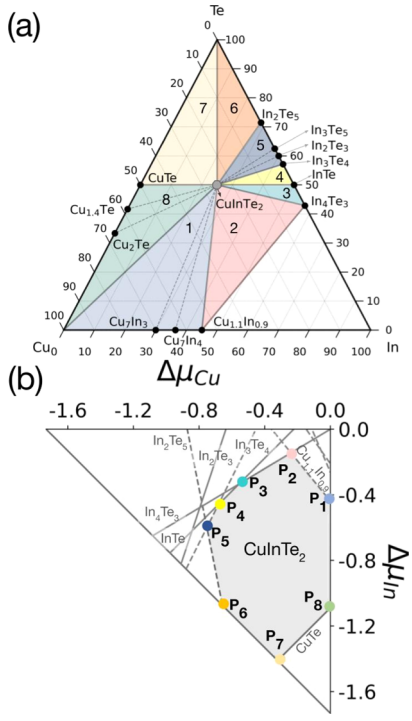

Figure 3. Phase stability diagrams of $CuInTe_2$ in (a) compositional and (b) chemical potential spaces. The boundaries of $\Delta\mu_i$ [$\Delta\mu_i$(poorest-i, richest-i)] for the three elemental phases i = Cu, In, and Te are $\Delta\mu_{Cu}$[−0.75, 0.00], $\Delta\mu_{In}$[−1.41, −0.14], and $\Delta\mu_{Te}$[−0.67, 0.00]. The color code indicates the direct link between compositional and chemical potential spaces, where three-phase equilibrium regions in (a) are directly linked to points in (b). Computational predictions combined with phase boundary mapping can then be used to guide the preparation of samples under synthetic control of chemical potentials, leading to high control and reproducibility of native carrier concentrations.

Besides pure Cu and Te phases, these regions are defined by six competing binaries: CuTe, $Cu_{11}In_9$, InTe, In_2Te_5, In_3Te_4, and In_4Te_3. We acknowledge that several phases are missing in our calculations, as their structures have not yet been characterized. Some examples are In_3Te_5, $CuIn_3Te_5$, $Cu_2In_4Te_7$, and $Cu_3In_7Te_{12}$.[24,27,51,52] We may then expect

https://dx.doi.org/10.1021/acs.chemmater.0c04041
Chem. Mater. 2021, 33, 359–369

some level of inaccuracy at the phase boundaries calculated here, with a direct impact on our predicted carrier concentrations. Additional sources of inaccuracy can arise depending on the method used to compute formation enthalpies of the main compound and competing phases (Supporting Information Figure S2).

Samples can then be prepared under synthetic control of chemical potentials, as areas representing three-phase equilibria in compositional space correspond to well-defined points in chemical potential space. As an example, the light blue triangular area 1 in Figure 3a denotes a three-phase equilibrium region between $CuInTe_2$, the elemental phase of copper, and $Cu_{11}In_9$. This corresponds to point $\mathbf{P}_1$ in Figure 3b, defined by the intersection between the stability lines of Cu and $Cu_{11}In_9$ with $CuInTe_2$. Preparation of multiphase samples that incorporate trace impurities of Cu and $Cu_{11}In_9$ with $CuInTe_2$ fix the μ_i to those of $\mathbf{P}_1$, and thus the defect formation energies and equilibrium concentrations. The same approach can be applied to explore the diverse thermodynamic space over the whole boundary of the host material, resulting in high control of dominant native defects and carrier concentrations.

Native Defects. Figure 4a–d shows the defect formation energies $\Delta H(D,q)$ of intrinsic defects D in their relevant charge states q plotted as a function of the Fermi energy E_F under four different sets of chemical potentials. E_F ranges between the VBM and the CBM, that is, within the band gap region. The equilibrium position of the Fermi energy E_F^{eq} is determined by the charge neutrality condition eq 7.

As discussed previously, the computed band gap of 0.97 eV using the HSE06 hybrid functional is reduced when SOC effects are taken into account. The resulting band edge shift of 0.24 eV is highlighted by the (vertical) gray area. This shift sets a band gap energy of 0.73 eV, shown by the white region.

Although the relative formation energies vary across different regions of the chemical potential space, three defects always dominate in $CuInTe_2$: V_{Cu} and Cu_{In}, which act as electron acceptors, thereby promoting p-type behavior, and In_{Cu}, which donates electrons to the host material, thereby contributing to decreasing the hole concentration. It is clear that the persistent p-type behavior of $CuInTe_2$ under Cu-poor conditions is a result of a high concentration of copper vacancies that increases the hole concentration. This is commonly observed in $CuInTe_2$ and related Cu-containing DLS materials. To decrease the hole concentration, an alternative to suppress the formation of V_{Cu} is to grow the sample under Cu-rich conditions. Excess of copper, however, facilitates the formation of Cu_{In} antisites, maintaining the p-type character of the system. As expected, In_{Cu} will be mostly favorable under In-rich and Cu-poor environments.

A favorable scenario for n-type doping requires then a careful balance between these three low-energy defects: the concentration of V_{Cu} and Cu_{In} should be minimized while maximizing In_{Cu} defects. Our calculated defect diagrams suggest that Cu- and In-rich conditions (Figure 4a,b) are the ideal place to grow $CuInTe_2$ to achieve n-type carriers via extrinsic dopants. Other sets of chemical potential will result in V_{Cu} and Cu_{In} acting as killer native acceptors, strongly preventing n-type doping (both intrinsically and extrinsically).

The carrier concentrations resulting from the equilibrium between intrinsic defects in $\mathbf{P}_1$, $\mathbf{P}_2$, $\mathbf{P}_5$, and $\mathbf{P}_7$ are shown in Figure 4e. High hole concentrations of the order of 10^{18} h cm^{-3} are predicted for a Cu-poor environment ($\mathbf{P}_5$) when Cu vacancies have low formation energy. Under Cu-rich conditions ($\mathbf{P}_1$), the hole concentrations drop to $\sim 10^{17}$ h cm^{-3}, maintaining a relatively high concentration. Such predicted concentrations are in good agreement with experimental measurements, as discussed in the Native Defects and Electronic Properties section, showing differences by ca. 1 order of magnitude. As mentioned previously, such discrepancy can arise from inaccuracies of the computed phase boundaries (Supporting Information Figures S2 and S3).

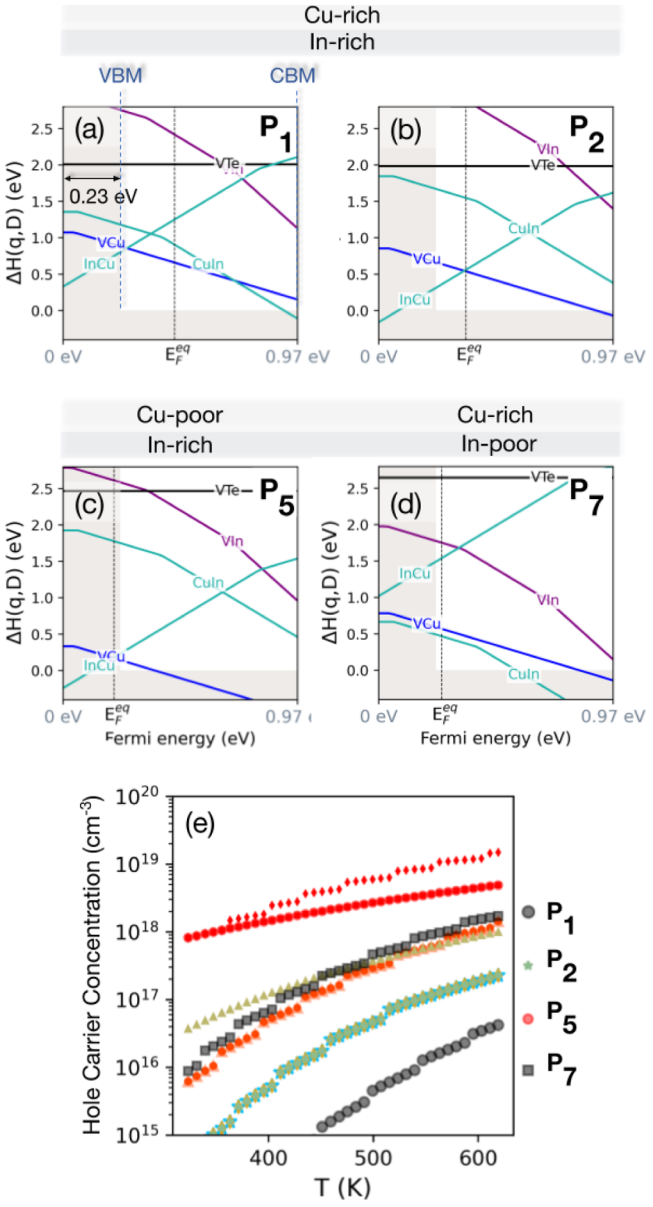

Figure 4. Defect formation energy as a function of Fermi energy for native vacancies and antisites in $CuInTe_2$ under four different growth environments (a) $\mathbf{P}_1$, (b) $\mathbf{P}_2$, (c) $\mathbf{P}_5$, and (d) $\mathbf{P}_7$ according to Figure 3b. The band edge shift of 0.23 eV when spin-orbit coupling (SOC) effects are taken into account is highlighted by the (vertical) gray area. This shift sets a band gap of 0.73 eV, shown in the white region. Over the whole stability region, three native defects always dominate, that is V_{Cu} and Cu_{In} that act as electron acceptors and the donor In_{Cu}. (e) Predicted carrier concentrations for three-phase equilibrium regions as marked in Figure 3b. Colored curves can be directly compared to the experimental results in Figure 5a, as discussed in the Native Defects and Electronic Properties section.

https://dx.doi.org/10.1021/acs.chemmater.0c04041
Chem. Mater. 2021, 33, 359–369

Synthesis. To test the effects of different stoichiometries on $CuInTe_2$, samples were prepared both on- and off-stoichiometry through the melting and hot pressing procedure described in the Methods section. The procedure yielded polycrystalline discs with densities >95% of the theoretical density of $CuInTe_2$. Several on-stoichiometric samples were synthesized, showing a consistent baseline with minimal hysteresis for the $CuInTe_2$ high-temperature thermoelectric properties (Supporting Information Figures S4−S9). The off-stoichiometric $CuInTe_2$ samples were made within 5% of the on-stoichiometric $CuInTe_2$. The nominal sample stoichiometries and densities are listed in the Supporting Information Table S2 and the experimentally determined sample compositions are shown in the Supporting Information Figures S25−S38. Differences between the nominal and measured sample compositions can be attributed to as detailed in the Supporting Information Figure S24.

As intended, X-ray diffraction of the samples shown in the Supporting Information Figure S11 indicates that samples are predominately the desired chalcopyrite phase with trace impurity phases present. Within the phase boundary mapping approach, achieving trace impurities is desirable as they pin the elemental chemical potential but are sufficiently dilute as to not require effective medium theory for transport analysis. While the full Cu−In−Te phase diagram is not established, particularly with respect to phase equilibria, the observed impurity phases follow the expectations created by deliberate off-stoichiometry (Supporting Information Figures S12−S14). Elemental tellurium appears in samples that are tellurium-rich; likewise, samples along the InTe tie-line exhibit InTe as a secondary phase. Samples on the copper-rich side contain either pure copper or copper telluride phases, as appropriate. Phase identification on the indium-rich side is challenging as the Cu−In binary phase diagram contains several high-temperature phases that melt incongruently; furthermore, not all phases have established crystal structures.[53] Some trace peaks appear consistently in all samples, indicating the presence of an external impurity that is not related to the ternary phase diagram. Collectively, these syntheses lead to a broad distribution of chalcopyrite stoichiometries and associated defect concentrations.

Native Defects and Electronic Properties. We establish a baseline for the composition-dependent properties using the nominally on-stoichiometric $CuInTe_2$ carrier concentration. The on-stoichiometric sample shows a carrier concentration of 2×10^{18} cm^{-3} at 323 K that is initially temperature-independent. Carrier activation begins to occur at 473 K, eventually reaching 8×10^{18} cm^{-3} at 623 K. Duplicate on-stoichiometric samples (Supporting Information Figure S6) show behavior that is very similar to the data shown in Figure 5. These repeatable property measurements of different on-stoichiometric samples give confidence that our synthesis methods provide good control of sample composition.

Compared to the baseline stoichiometric samples, both Cu-deficient and strongly copper-rich compositions show a significant increase in carrier concentration. Cu-deficient samples were able to reach room-temperature carrier concentrations of $\sim 3 \times 10^{19}$ h^+ cm^{-3}. These results were consistent internally across the three samples $Cu_{0.9}InTe_2$, $Cu_{0.88}In_{1.02}Te_2$, and $Cu_{0.95}In_{0.95}Te_2$. Cu deficiency has been well studied as a route to increasing the carrier concentration of $CuInTe_2$,[17,24,26−28,54] while comparatively few works have demonstrated a carrier concentration increase as a result of

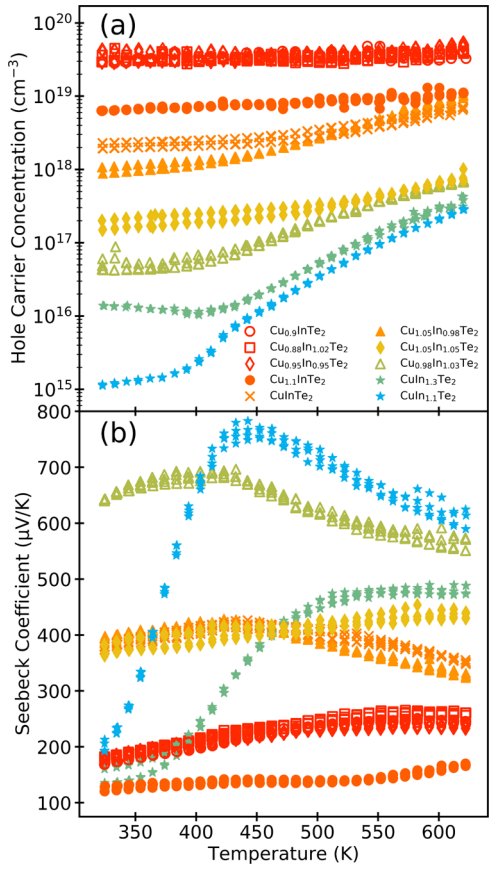

Figure 5. (a) High-temperature carrier concentration of $CuInTe_2$ exhibits nearly 5 orders of magnitude due to variations in stoichiometry. (b) Temperature-dependent Seebeck coefficients rising at low temperature and falling at high temperature due to carrier activation.

excess copper.[29,55] The most Cu-rich sample has a room-temperature carrier concentration of $\sim 6 \times 10^{18}$ h^+ cm^{-3}. As the temperature of these high carrier-concentration samples increases, the nearly constant carrier concentration is evidence of extrinsic behavior and a substantial band gap.[56] Despite clearly different mechanisms for the creation of h^+, the temperature-dependences of the carrier concentrations are effectively indistinguishable. With modest Cu richness, the carrier concentration in fact drops slightly from the on-stoichiometric $CuInTe_2$ sample. The high-temperature properties likewise show an earlier onset of minority carrier activation with respect to temperature. These results will be discussed in the context of the defect calculations after considering In-rich samples.

The low carrier concentration ($<10^{18}$ cm^{-3}) samples of Figure 5 are consistently samples with high indium concentration. The most indium-rich samples, $CuIn_{1.1}Te_2$ and $CuIn_{1.3}Te_2$, show the lowest carrier concentrations at 1×10^{15} and 1×10^{16} cm^{-3}, respectively. Adjusting the stoichiometry perturbation away from elemental indium (i.e., $Cu_{0.98}In_{1.03}Te_2$ lies on the tie-line with InTe, $Cu_{1.05}In_{1.05}Te_2$ lies slightly on the tie line of $Cu_{11}In_9$), one finds carrier concentrations between 6×10^{16} to 2×10^{17} cm^{-3}. These low carrier concentration samples show significant cross-gap activation with increasing temperature after an initial extrinsic regime. Between 400 and 550 K, cross-gap activation can be identified by the onset of exponential increases in carrier

https://dx.doi.org/10.1021/acs.chemmater.0c04041
Chem. Mater. 2021, 33, 359−369

concentration. While these low carrier concentration samples each have differing carrier concentrations, the total change in carrier concentration with respect to temperature is quite similar ($\sim 10^{17}$ cm^{-3}). The consistency between these low carrier concentration samples suggests that they share a similar electronic structure.

In light of these experimental results, we return to the defect calculations presented above. There are three dominant defects that affect the carrier concentration in the $CuInTe_2$ system. The most prevalent defect is V_{Cu} that acts as an electron acceptor thereby increasing the hole carrier concentration.[17,24,26,28] Figure 4 shows that in all cases, V_{Cu} has low formation energy. The low formation energy is consistent with the p-type behavior and the high carrier concentration of the copper-deficient samples in Figure 6.

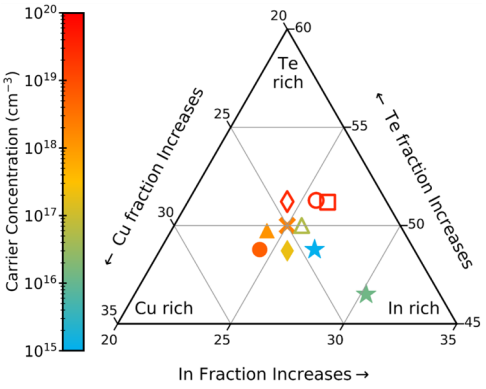

Figure 6. Heat map of carrier concentration and composition showing low carrier concentration for indium-rich samples.

Similarly, Cu_{In} also contributes to an increasing hole carrier concentration. The higher formation energy of Cu_{In} compared to V_{Cu} explains the lower carrier concentration of $Cu_{1.1}InTe_2$ in comparison to $Cu_{0.9}InTe_2$. As there is a trade-off between the concentrations of V_{Cu} and Cu_{In} with $\Delta\mu_{Cu}$, the carrier concentration minimum may not be at the nominally stoichiometric composition; rather, the sample that was grown slightly Cu-rich showed the lowest carrier concentration.

The last defect is In_{Cu}, which acts as an electron donor and thus reduces the hole carrier concentration. The donor effects of In_{Cu} are consistent with the low carrier concentrations of the indium-rich samples shown in Figure 6. This distribution of defects about $CuInTe_2$ indicates that a map of the carrier concentration with respect to composition is a nonlinear surface created by a balance between the V_{Cu}, In_{Cu}, and Cu_{In} defects. To minimize the hole concentration, not only must one maximize In_{Cu} but also minimize both Cu_{In} and V_{Cu}; this delicate balance happens only in a narrow synthetic regime.

The Seebeck coefficients for all samples are well correlated with the carrier concentration. At high carrier concentrations, the Seebeck coefficient is consistent with a heavily doped semiconductor (<300 μV/K). Extrapolation of the Seebeck coefficients of these high carrier concentration samples in the Supporting Information Figure S16 shows an intercept of ~30 μV/K at 0 K, indicating a near-linear temperature dependence until bipolar effects begin at 450 K. This linear behavior suggests that a parabolic band approximation will suitably model the Seebeck coefficient. For the degenerate samples, the density of states effective mass (m^*_{DOS}) is estimated to be 0.4–0.6 m_e using a single parabolic band approximation and the assumption of acoustic phonon scattering, compared to electronic structure calculations suggesting a valence band m^*_{DOS} of 0.65 m_e. This assumption is supported by the temperature dependence of the Hall mobility, reported below.

The high Seebeck coefficient values (300–800 μV/K) observed for the low carrier concentration samples show significant evidence of bipolar behavior. We note that the band masses and mobilities of the valence and conduction bands are expected to be quite distinct, exacerbating the quantitative analysis of these results.[57] It is possible that chemistry within the sample is slightly changing; at these low carrier densities, minute changes in stoichiometry will dramatically affect the magnitude of the Seebeck coefficient. However, the absence of hysteresis in these measurements suggests that changes in local chemistry (i.e., the ion mobility of Cu) would have to occur on a timescale shorter than the measurement cycle.

Resistivity and Mobility. The resistivity of the samples (Figure 7) finds room-temperature values ranging from 3 to

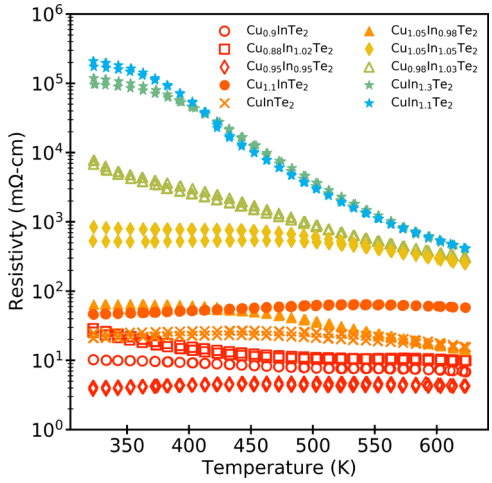

Figure 7. High-temperature resistivity of $CuInTe_2$ decreasing with respect to temperature, driven primarily by an increasing carrier concentration.

10^5 mΩ cm. The highest carrier concentration materials show nearly constant resistivity with temperature; such behavior is similar to metals in the regime of strong defect scattering. The low and moderate carrier density samples show the classic drop in resistivity found in intrinsic semiconductors; this is driven primarily by carrier excitation across the band gap leading to ×10–100 increase in carrier density. The magnitude of the band gap is thus estimated from the temperature-dependence of the resistivity (Supporting Information Figure S10), under the approximation of temperature-independent mobility. For the lowest carrier concentration samples (indium-rich), the band gap is extrapolated to be between 0.85 and 0.95 eV. This range of band gaps is quite close to the calculated values.

The combination of Hall effect and resistivity measurements allows for the Hall mobility (Figure 8) to be extracted. Typically, this is done within a single carrier-type regime and the approximation of parabolic bands, leading to the classic expression $R_H = 1/ne$. For samples with 1×10^{18} cm^{-3} and above, the carrier concentration is largely constant with temperature and the above approximations are expected to hold. In the following, we begin by analyzing the results for high carrier concentration samples; to address the lower carrier

https://dx.doi.org/10.1021/acs.chemmater.0c04041
Chem. Mater. 2021, 33, 359–369

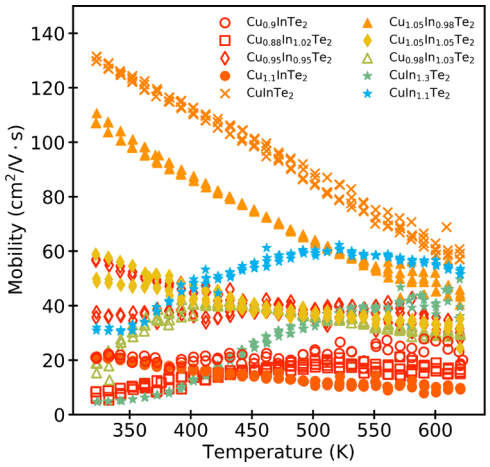

Figure 8. Mobility showing different behavior depending on the defect concentration. Moderate carrier concentrations show high mobility, while high carrier concentrations show low mobility as a result of vacancy scattering.

concentration sample mobility, a two-band model is then employed. Within the high carrier concentration samples, the magnitude and temperature dependence of the mobility is a strong function of defect concentration. (Figure 8) shows that the mobility of the stoichiometric sample is quite high at room temperature (~130 $cm^2/V{\cdot}s$) and decays with temperature. Such behavior is indicative of electron-phonon scattering. Similar behavior is seen in the $Cu_{1.05}In_{0.98}Te_2$ sample which has a slightly lower carrier concentration. However, at higher carrier concentrations, the mobility is significantly reduced (5–20 $cm^2/V{\cdot}s$) and shows nearly temperature-independent behavior. This occurs in both Cu-rich and -poor samples and is indicative of strong point defect scattering.[24,26] In parallel with the increased point defect scattering in these high carrier concentration samples, the scattering rate from acoustic phonons is expected to scale with $\tau \propto n^{-1/3}$ at high carrier densities.

Within the high carrier concentration samples, there is a significant mobility difference between the tellurium-rich ($Cu_{0.95}In_{0.95}Te_2$) and copper-deficient ($Cu_{0.88}In_{1.02}Te_2$ and $Cu_{0.9}InTe_2$) samples even though they have nearly the same carrier concentrations (3×10^{18} h^+ cm^{-3}) and similar microstructures (Supporting Information Figures S25, S26, S29). The copper-deficient samples likely contain a higher concentration of V_{Cu} that contributes to increased scattering and thus reduced mobility. However, the tellurium-rich sample has higher mobility as a result of a balance between V_{Cu} and Cu_{In} acceptor defects.

The increase in hole carrier concentration of the intrinsic materials shown in Figure 5 must also mean that electrons are being promoted to the conduction band. Given that the intrinsic samples already have a very low carrier hole concentration, such behavior could lead to parallel transport of electrons and holes at high temperatures. This bipolar conduction could lead to an incorrect analysis of the high-temperature Hall coefficient.

Estimating the room-temperature mobility of the low carrier concentration (<10^{18} cm^{-3}) samples with a single band model yields values below 60 $cm^2/V{\cdot}s$. The In_{Cu} defect may act as a scattering site, as this is a high-concentration defect in all of these samples ($CuIn_{1.1}Te_2$, $CuIn_{1.3}Te_2$, $Cu_{0.98}In_{1.03}Te_2$, and $Cu_{1.05}In_{1.05}Te_2$). Additionally, mobility could be affected by microstructural differences as shown in the Supporting Information Figures S25–S38. At high temperatures, the single band model approximations shown in (Figure 8) is likely incorrect; a discussion of multiband mobility analysis is presented in the Supporting Information.

Phonons. The calculated phonon dispersion curves for $CuInTe_2$ are shown in Figure 9. The acoustic branches' speed

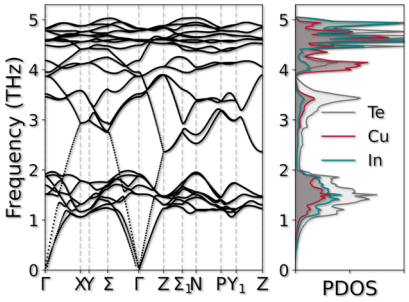

Figure 9. Phonon dispersion of bulk $CuInTe_2$ in the chalcopyrite structure shows low-frequency optical modes crossing through the acoustic branches. The elementally decomposed PDOS highlights the role that Te plays in these optical modes.

of sound is consistent with experimental measurements of the longitudinal and transverse speed of sound measurements (Supporting Information Figures S17–S18) on polycrystalline samples. There are two high density of state regions, the first between 1 and 2 THz and the second between 4 and 5 THz. The low-frequency optical bands show a high degree of overlap with the acoustic branches, similar to a phonon dispersion of a clathrate material with strongly scattering rattlers. However, these low-frequency optical modes involve all of the constituent atoms rather than just a rattling atom. These low-frequency bands provide scattering pathways for high-velocity acoustic phonons. However, these optical modes still have significant group velocity (Supporting Information Figure S15). At high frequencies (4–5 THz), a high density of state region appears with significantly flatter, lower group velocity bands. These optical bands remain within the energy range for acoustic phonon scattering.[58]

From the phonon density of states (PDOS), the contributions of Cu, In, and Te states are shown. Between 1 and 2 THz, there is a significant contribution from tellurium states, likely driven by its high mass. However, there is still a high number of copper and indium states that is involved in these modes as well, suggesting a strong coupling between all of the atoms, as opposed to an isolated rattler. Similarly, a high density of tellurium states peak exists between 3 and 4 THz, and some tellurium states are even higher. Within the chalcopyrite structure, tetrahedral coordination between all of the atoms is likely to contribute to mixing in the PDOS. Specifically, all cations have tellurium as nearest neighbors. In comparison to our prior work on quaternary DLSs, the PDOS shown in Figure 9 is nearly indistinguishable from $Cu_2CdSnTe_4$ (treating Cd and Sn as nearly equivalent to In).[57]

Thermal Properties and *zT*. High-temperature lattice thermal conductivity shown in Figure 10 indicates an overall decline with increasing temperature for all samples. The electronic component of the thermal conductivity (Supporting Information Figure S21) is <15% for all samples, leaving a lattice component (κ_L) that follows the same trend. This T^{-1} temperature dependence is typically ascribed to phonon–

https://dx.doi.org/10.1021/acs.chemmater.0c04041
Chem. Mater. 2021, 33, 359–369

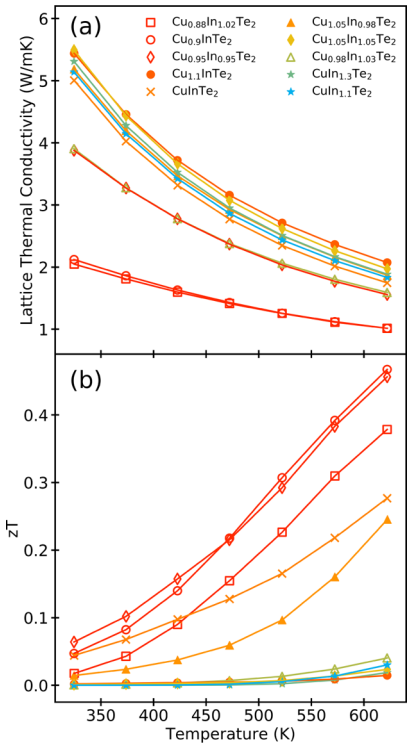

Figure 10. (a) Lattice thermal conductivity showing a reduction with temperature as a result of electron−phonon scattering. The copper-deficient samples have a significantly lower lattice thermal conductivity, likely as a result of point-defect scattering resulting from copper vacancies. (b) Thermoelectric figure of merit indicating the highest performance for the copper-deficient samples. The samples $Cu_{0.9}InTe_2$ and $Cu_{0.95}In_{0.95}Te_2$ have differing lattice thermal conductivities but similar figures of merit.

phonon scattering.[59] Given that the variation in $CuInTe_2$ stoichiometry is not particularly extreme, there is a significant spread in κ_L. This is consistent with prior studies of copper-deficient $CuInTe_2$ where copper deficiency led to similar decreases in thermal conductivity.[24,26] Here, we have the opportunity to compare the impact of In_{Cu} and Cu_{In} defects along with the already studied V_{Cu}.

Consistent with prior results, the low thermal conductivity of copper-deficient samples suggests that copper vacancies contribute strongly to phonon scattering. The copper-deficient samples, $Cu_{0.9}InTe_2$ and $Cu_{0.88}In_{1.02}Te_2$, have the highest concentration of copper vacancies and thus a lower thermal conductivity. With slightly less copper deficiency, the samples $Cu_{0.95}In_{0.95}Te_2$ and $Cu_{0.98}In_{1.03}Te_2$ show an intermediate range of thermal conductivity. The trend of thermal conductivity is similar to the mobility in that the highest vacancy concentrations have the lowest mobility. As the compositions move away from the copper-deficient regions, the thermal conductivity increases, indicating that the Cu_{In} and In_{Cu} defects are comparatively weak scatterers compared to the vacancy. Further complicating matters, the In−Te-rich side of the phase diagram is known to contain ternaries that are ordered vacancy chalcopyrites (e.g., $CuIn_5Te_8$ and $CuInTe_3Te_5$) as well as disordered, cation vacancy-rich zinc blende compounds (e.g., $Cu_2In_4Te_7$).[24,27] In both cases, room-temperature κ_L values of 1.1−1.3 W m^{-1} K^{-1} are observed. Analysis of the strength of the V_{Cu} scattering may be additionally complicated by the formation of V_{Cu} clusters that are stronger scatterers of the acoustic phonons.

$CuInTe_2$ shows zT values that are primarily dependent on carrier concentration as shown in Figure 10b. Samples with the highest zT have carrier concentrations of $\sim 3 \times 10^{19}$ h^+ cm^{-3}; all of these compounds have a copper deficiency. Compared to the best-performing samples in the prior literature, the highest zT values herein are equivalent for a given temperature. Such materials, when measured to higher temperatures, have shown zT in excess of unity. It is interesting that such prior efforts have utilized extrinsic dopants and nanostructuring to achieve similar results.[15,18] All other samples herein are too resistive to exhibit significant zT.

CONCLUSIONS

Thermoelectric research on $CuInTe_2$ has previously focused on optimization of the figure of merit through the use of external dopants without a baseline understanding of the native material. Such one-dimensional studies create a gap in the knowledge of fundamental defect chemistry that could be used for more effective optimization. In this work, we highlight that the optimization of the carrier concentration and the figure of merit for $CuInTe_2$ can be tuned solely by the native defects. Calculations paired with intentionally off-stoichiometric syntheses were used to identify the dominant defects in $CuInTe_2$ and their impact on transport properties.

First-principles hybrid DFT calculations suggest a relatively large stability region for this ternary semiconductor, indicating that native carrier concentrations can be largely controllable under diverse growth conditions. Calculated defect formation energies of native defects in the dilute limit reveal that three point defects dominate in $CuInTe_2$: the acceptors V_{Cu} and Cu_{In} and the donor In_{Cu}. Such a result elucidates the persistent p-type character of $CuInTe_2$, frequently reported in the literature, caused by the constant presence of a "killer" native acceptor (V_{Cu} in Cu-poor and Cu_{In} in Cu-rich environments). A precise balance between these dominant defects is then required to achieve a favorable scenario for n-type dopability. Our calculations indicate that such a scenario can indeed be accessed in specific In- and Cu-rich growth conditions.

High density on- and off-stoichiometry samples produced by traditional methods confirm the presence of the aforementioned dominant defects. Copper-deficient samples are found to have a high hole carrier concentration as a result of the V_{Cu}, while indium-rich samples show the lowest hole carrier concentration as a result of the In_{Cu} antisite defects. A moderately high carrier concentration is identified in copper-rich samples as a result of the Cu_{In} antisite defect. The mobility of copper-deficient samples suggests that copper vacancies are stronger scatterers in comparison to the Cu_{In} and In_{Cu} defects. Similar vacancy scattering behavior of phonons is identified by the low lattice thermal conductivity of the copper-deficient samples. Both the high carrier concentration and low lattice thermal conductivity of the copper-deficient $CuInTe_2$ samples show that the thermoelectric performance of the p-type material can be improved without the use of external dopants and microstructure engineering. The low carrier concentration samples indicate that n-type dopability will be most successful when synthesis is performed in an indium-rich environment. Ultimately, the simple act of native defect engineering yields a thermoelectric performance equivalent to prior efforts in heavily engineered p-$CuInTe_2$ while providing a path toward n-type dopability.

https://dx.doi.org/10.1021/acs.chemmater.0c04041
Chem. Mater. 2021, 33, 359−369

■ ASSOCIATED CONTENT

Supporting Information

The Supporting Information is available free of charge at https://pubs.acs.org/doi/10.1021/acs.chemmater.0c04041.

Computed formation enthalpies of $CuInTe_2$ and competing phases; phase stability diagrams; theoretical carrier concentration; temperature-dependent Seebeck coefficients, resistivity of the nominally on-stoichiometric samples, carrier concentrations, mobility showing linearly decreasing behavior, lattice thermal conductivity, and zT; band gap calculated from resistivity; X-ray diffraction of the on-stoichiometric samples, copper-deficient samples, copper-rich samples, and indium-rich samples; phonon group velocity of $CuInTe_2$; linear fit of the copper-deficient Seebeck coefficients; shear and longitudinal sound velocities; multiband simulation properties; experimental, 1-band, and 2-band hole carrier concentrations; band gap calculated from carrier concentration; electronic, lattice, and total thermal conductivity; nominal compositions compared against the actual compositions; backscatter SEM images; range of grain sizes for each sample; lattice parameters and cell volume computed from Rietveld refinements of XRD patterns (PDF)

■ AUTHOR INFORMATION

Corresponding Authors

Jesse M. Adamczyk − *Department of Physics, Colorado School of Mines, Golden 80401, Colorado, United States;* orcid.org/0000-0002-5508-7284; Email: adamczyk@mymail.mines.edu

Lídia C. Gomes − *Department of Mechanical Science and Engineering, University of Illinois Urbana Champaign, Champaign 61820, Illinois, United States;* Email: lidiacarvalhog@gmail.com

Authors

Jiaxing Qu − *Department of Mechanical Science and Engineering, University of Illinois Urbana Champaign, Champaign 61820, Illinois, United States;* orcid.org/0000-0002-3304-4996

Grace A. Rome − *Department of Materials and Metallurgical Engineering, Colorado School of Mines, Golden 80401, Colorado, United States*

Samantha M. Baumann − *Department of Materials and Metallurgical Engineering, Colorado School of Mines, Golden 80401, Colorado, United States*

Elif Ertekin − *Department of Mechanical Science and Engineering, University of Illinois Urbana Champaign, Champaign 61820, Illinois, United States;* orcid.org/0000-0002-7816-1803

Eric S. Toberer − *Department of Physics, Colorado School of Mines, Golden 80401, Colorado, United States*

Complete contact information is available at: https://pubs.acs.org/10.1021/acs.chemmater.0c04041

Author Contributions

‖J.M.A. and L.C.G. is shared as a result of equal intellectual contributions.

Notes

The authors declare no competing financial interest.

■ ACKNOWLEDGMENTS

This work was funded primarily with support from the National Science Foundation (NSF) via grants DMR1729594 and DMR1729149. Additional funding was provided by Advanced Research Projects Agency Energy (ARPA-E) via grant DE-AR0000840.

■ REFERENCES

(1) Dafinei, I.; Fasoli, M.; Ferroni, F.; Mihokova, E.; Orio, F.; Pirro, S.; Vedda, A. Low Temperature Scintillation in ZnSe Crystals. *IEEE Trans. Nucl. Sci.* **2010**, *57*, 1470−1474.

(2) Chen, W. R.; Huang, C. J. ZnSe-based mixed-color LEDs. *IEEE Photon. Technol. Lett.* **2004**, *16*, 1259−1261.

(3) Kerr, L. L.; Li, S. S.; Johnston, S. W.; Anderson, T. J.; Crisalle, O. D.; Kim, W. K.; Abushama, J.; Noufi, R. N. Investigation of defect properties in $Cu(In,Ga)Se_2$ solar cells by deep-level transient spectroscopy. *Solid-State Electron.* **2004**, *48*, 1579−1586.

(4) Lany, S.; Zunger, A. Light- and bias-induced metastabilities in $Cu(In,Ga)Se_2$ based solar cells caused by the $(V_{Se}$-$V_{Cu})$ vacancy complex. *J. Appl. Phys.* **2006**, *100*, 113725.

(5) Contreras, M. A.; Egaas, B.; Ramanathan, K.; Hiltner, J.; Swartzlander, A.; Hasoon, F.; Noufi, R. Progress toward 20% efficiency in $Cu(In,Ga)Se_2$ polycrystalline thin-film solar cells. *Prog. Photovoltaics* **1999**, *7*, 311−316.

(6) Palmiotti, E.; Johnston, S.; Gerber, A.; Guthrey, H.; Rockett, A.; Mansfield, L.; Silverman, T. J.; Al-Jassim, M. Identification and analysis of partial shading breakdown sites in $CuIn_xGa_{(1-x)}Se_2$ modules. *Sol. Energy* **2018**, *161*, 1−5.

(7) Lugueva, N. V.; Luguev, S. M.; Dunaev, A. A. Thermal conductivity of polycrystalline zinc selenide. *Phys. Solid State* **2003**, *45*, 449−452.

(8) Irie, T.; Endo, S.; Kimura, S. Electrical Properties of p- and n-Type $CuInSe_2$ Single Crystals. *Jpn. J. Appl. Phys.* **1979**, *18*, 1303−1310.

(9) Mandel, L.; Tomlinson, R.; Hampshire, M.; Neumann, H. Electrical properties of $CuGaSe_2$ single crystals. *Solid State Commun.* **1979**, *32*, 201−204.

(10) Dinca, S. A.; Schiff, E. A.; Egaas, B.; Noufi, R.; Young, D. L.; Shafarman, W. N. Hole drift mobility measurements in polycrystalline $CuIn_{1-x}Ga_xSe_2$. *Phys. Rev. B: Condens. Matter Mater. Phys.* **2009**, *80*, 235201.

(11) Werner, J. H.; Mattheis, J.; Rau, U. Efficiency limitations of polycrystalline thin film solar cells: case of $Cu(In,Ga)Se_2$. *Thin Solid Films* **2005**, *480*−*481*, 399−409.

(12) Ortiz, B. R.; Gordiz, K.; Gomes, L. C.; Braden, T.; Adamczyk, J. M.; Qu, J.; Ertekin, E.; Toberer, E. S. Carrier density control in $Cu_2HgGeTe_4$ and discovery of Hg_2GeTe_4 via phase boundary mapping. *J. Mater. Chem. A* **2019**, *7*, 621−631.

(13) Plirdpring, T.; Kurosaki, K.; Kosuga, A.; Day, T.; Firdosy, S.; Ravi, V.; Snyder, G. J.; Harnwunggmoung, A.; Sugahara, T.; Ohishi, Y.; Muta, H.; Yamanaka, S. Chalcopyrite $CuGaTe_2$: A High-Efficiency Bulk Thermoelectric Material. *Adv. Mater.* **2012**, *24*, 3622−3626.

(14) Liu, R.; Xi, L.; Liu, H.; Shi, X.; Zhang, W.; Chen, L. Ternary compound $CuInTe_2$: a promising thermoelectric material with diamond-like structure. *Chem. Commun.* **2012**, *48*, 3818−3820.

(15) Luo, Y.; Yang, J.; Jiang, Q.; Li, W.; Zhang, D.; Zhou, Z.; Cheng, Y.; Ren, Y.; He, X. Progressive Regulation of Electrical and Thermal Transport Properties to High-Performance $CuInTe_2$ Thermoelectric Materials. *Adv. Energy Mater.* **2016**, *6*, 1600007.

(16) Carr, W. D.; Morelli, D. T. Influence of doping and solid solution formation on the thermoelectric properties of chalcopyrite semiconductors. *J. Alloys Compd.* **2015**, *630*, 277−281.

(17) Yang, J.; Chen, S.; Du, Z.; Liu, X.; Cui, J. Lattice defects and thermoelectric properties: the case of p-type $CuInTe_2$ chalcopyrite on introduction of zinc. *Dalton Trans.* **2014**, *43*, 15228−15236.

(18) Luo, Y.; Yang, J.; Jiang, Q.; Li, W.; Xiao, Y.; Fu, L.; Zhang, D.; Zhou, Z.; Cheng, Y. Large enhancement of thermoelectric perform-

ance of $CuInTe_2$ via a synergistic strategy of point defects and microstructure engineering. *Nano Energy* **2015**, *18*, 37−46.
(19) Shen, J.; Chen, Z.; lin, S.; Zheng, L.; Li, W.; Pei, Y. Single parabolic band behavior of thermoelectric p-type $CuGaTe_2$. *J. Mater. Chem. C* **2016**, *4*, 209−214.
(20) Wasim, S. M.; Marcano, G.; Pérez, G. S. Electrical properties of $CuGaTe_2$. *Phys. Status Solidi A* **1983**, *78*, 423−430.
(21) Qin, Y.; Qiu, P.; Liu, R.; Li, Y.; Hao, F.; Zhang, T.; Ren, D.; Shi, X.; Chen, L. Optimized thermoelectric properties in pseudocubic diamond-like $CuGaTe_2$ compounds. *J. Mater. Chem. A* **2016**, *4*, 1277−1289.
(22) Shen, J.; Zhang, X.; Lin, S.; Li, J.; Chen, Z.; Li, W.; Pei, Y. Vacancy scattering for enhancing the thermoelectric performance of $CuGaTe_2$ solid solutions. *J. Mater. Chem. A* **2016**, *4*, 15464−15470.
(23) Shen, J.; Zhang, X.; Chen, Z.; Lin, S.; Li, J.; Li, W.; Li, S.; Chen, Y.; Pei, Y. Substitutional defects enhancing thermoelectric $CuGaTe_2$. *J. Mater. Chem. A* **2017**, *5*, 5314−5320.
(24) Kosuga, A.; Higashine, R.; Plirdpring, T.; Matsuzawa, M.; Kurosaki, K.; Yamanaka, S. Effects of the Defects on the Thermoelectric Properties of Cu−In−Te Chalcopyrite-Related Compounds. *Jpn. J. Appl. Phys.* **2012**, *51*, 121803.
(25) Plirdpring, T.; Kurosaki, K.; Kosuga, A.; Ishimaru, M.; Harnwunggmoung, A.; Sugahara, T.; Ohishi, Y.; Muta, H.; Yamanaka, S. Effect of the Amount of Vacancies on the Thermoelectric Properties of Cu-Ga-Te Ternary Compounds. *Mater. Trans.* **2012**, *53*, 1212−1215.
(26) Xia, Z.; Wang, G.; Zhou, X.; Wen, W. Effect of the Cu vacancy on the thermoelectric performance of p-type $Cu_{1-x}InTe_2$ compounds. *Ceram. Int.* **2017**, *43*, 16276−16282.
(27) Plirdpring, T.; Kurosaki, K.; Kosuga, A.; Ishimaru, M.; Ohishi, Y.; Muta, H.; Yamanaka, S. High-temperature thermoelectric properties of $Cu_2In_4Te_7$. *Phys. Status Solidi RRL* **2012**, *6*, 154−156.
(28) Yan, Y.; Lu, X.; Wang, G.; Zhou, X. zT = 1.1 in $CuInTe_2$ Solid Solutions Enabled by Rational Defect Engineering. *ACS Appl. Energy Mater.* **2020**, *3*, 2039−2048.
(29) Lacruz, A.; Rincón, C.; Pérez, G. S.; Wasim, S. M. Electrical and optical properties of $CuInTe_2$ grown from near-stoichiometric compositions. *Prog. Cryst. Growth Char.* **1984**, *10*, 283−287.
(30) Yan, J.; Gorai, P.; Ortiz, B.; Miller, S.; Barnett, S. A.; Mason, T.; Stevanović, V.; Toberer, E. S. Material descriptors for predicting thermoelectric performance. *Energy Environ. Sci.* **2015**, *8*, 983−994.
(31) Wasim, S. M.; Albornóz, J. G. Electrical and optical properties of n-and p-type $CuInTe_2$. *Phys. Status Solidi A* **1988**, *110*, 575−583.
(32) Kazmerski, L. L.; Juang, Y. J. Vacuum-deposited $CuInTe_2$ thin films: Growth, structural, and electrical properties. *J. Vac. Sci. Technol.* **1977**, *14*, 769−776.
(33) Kazmerski, L. L.; Shieh, C. C. Photoconductivity effects in $CuInS_2$, $CuInSe_2$ and $CuInTe_2$ thin films. *Thin Solid Films* **1977**, *41*, 35−41.
(34) Neumann, H.; Tomlinson, R. D.; Nowak, E.; Elliott, E.; Howarth, L. Electrical properties of As-grown $CuInTe_2$ single crystals. *Krist. Tech.* **1981**, *16*, K112−K114.
(35) Schön, J. H. Extrinsic doping of $CuGaSe_2$ single crystals. *J. Phys. D: Appl. Phys.* **2000**, *33*, 286.
(36) Ohno, S.; Imasato, K.; Anand, S.; Tamaki, H.; Kang, S. D.; Gorai, P.; Sato, H. K.; Toberer, E. S.; Kanno, T.; Snyder, G. J. Phase boundary mapping to obtain n-type Mg_3Sb_2-based thermoelectrics. *Joule* **2018**, *2*, 141−154.
(37) Lany, S.; Zunger, A. Accurate prediction of defect properties in density functional supercell calculations. *Model. Simulat. Mater. Sci. Eng.* **2009**, *17*, 084002.
(38) Freysoldt, C.; Grabowski, B.; Hickel, T.; Neugebauer, J.; Kresse, G.; Janotti, A.; Van de Walle, C. G. First-principles calculations for point defects in solids. *Rev. Mod. Phys.* **2014**, *86*, 253−305.
(39) Hohenberg, P.; Kohn, W. Inhomogeneous Electron Gas. *Phys. Rev.* **1964**, *136*, B864−B871.
(40) Kohn, W.; Sham, L. J. Self-Consistent Equations Including Exchange and Correlation Effects. *Phys. Rev.* **1965**, *140*, A1133−A1138.
(41) Kresse, G.; Furthmüller, J. Efficient Iterative Schemes for Ab Initio Total-Energy Calculations Using a Plane-Wave Basis Set. *Phys. Rev. B: Condens. Matter Mater. Phys.* **1996**, *54*, 11169−11186.
(42) Perdew, J. P.; Burke, K.; Ernzerhof, M. Generalized Gradient Approximation Made Simple. *Phys. Rev. Lett.* **1996**, *77*, 3865−3868.
(43) Krukau, A. V.; Vydrov, O. A.; Izmaylov, A. F.; Scuseria, G. E. Influence of the exchange screening parameter on the performance of screened hybrid functionals. *J. Chem. Phys.* **2006**, *125*, 224106.
(44) Blöchl, P. E. Projector Augmented-Wave Method. *Phys. Rev. B* **1994**, *50*, 17953−17979.
(45) Monkhorst, H. J.; Pack, J. D. Special points for Brillouin-zone integrations. *Phys. Rev. B* **1976**, *13*, 5188−5192.
(46) Ganose, A. M.; Jackson, A. J.; Scanlon, D. O. sumo: Command-line tools for plotting and analysis of periodic *ab initio* calculations. *J. Open Source Software* **2018**, *3*, 717.
(47) Parlinski, K.; Li, Z. Q.; Kawazoe, Y. First-Principles Determination of the Soft Mode in Cubic ZrO_2. *Phys. Rev. Lett.* **1997**, *78*, 4063−4066.
(48) Togo, A.; Tanaka, I. First principles phonon calculations in materials science. *Scr. Mater.* **2015**, *108*, 1−5.
(49) Iwanaga, S.; Toberer, E. S.; LaLonde, A.; Snyder, G. J. A high temperature apparatus for measurement of the Seebeck coefficient. *Rev. Sci. Instrum.* **2011**, *82*, 063905.
(50) Borup, K. A.; Toberer, E. S.; Zoltan, L. D.; Nakatsukasa, G.; Errico, M.; Fleurial, J.-P.; Iversen, B. B.; Snyder, G. J. Measurement of the electrical resistivity and Hall coefficient at high temperatures. *Rev. Sci. Instrum.* **2012**, *83*, 123902.
(51) Budanova, N. Y.; Skasyrskaya, E. Y. Phase diagram of the indium-tellurium system. *Inorg. Mater.* **1998**, *34*, 220−221.
(52) Arciniegas, G. E. D.; Guedez, E.; Sanchéz-Pérez, G.; Rincón, C.; Marroquin, G. Evidence of a new ordered vacancy crystal structure in the compound $Cu_3In_7Te_{12}$. *Matéria*, **2019**, *24*, e-12329, DOI: 10.1590/s1517-707620190001.0643.
(53) Subramanian, P. R.; Laughlin, D. E. The Cu-In (Copper-Indium) system. *Bull. Alloy Phase Diagrams* **1989**, *10*, 554−568.
(54) Zhang, S. B.; Wei, S.-H.; Zunger, A. Stabilization of ternary compounds via ordered arrays of defect pairs. *Phys. Rev. Lett.* **1997**, *78*, 4059.
(55) Wasim, S. M.; Porras, G. S.; Tomlinson, R. D. Some electrical characteristics of Cu- and In-doped $CuInTe_2$. *Phys. Status Solidi A* **1982**, *71*, 523−530.
(56) Qu, J.; Stevanovic, V.; Ertekin, E.; Gorai, P. Doping by design: finding new n-type dopable ABX_4 Zintl phases for thermoelectrics. *J. Mater. Chem. A* **2020**, *8*, 25306−25315.
(57) Ortiz, B. R.; Peng, W.; Gomes, L. C.; Gorai, P.; Zhu, T.; Smiadak, D. M.; Snyder, G. J.; Stevanović, V.; Ertekin, E.; Zevalkink, A.; et al. Ultralow thermal conductivity in diamond-like semiconductors: selective scattering of phonons from antisite defects. *Chem. Mater.* **2018**, *30*, 3395−3409.
(58) Broido, D. A.; Lindsay, L.; Reinecke, T. L. Ab initio study of the unusual thermal transport properties of boron arsenide and related materials. *Phys. Rev. B: Condens. Matter Mater. Phys.* **2013**, *88*, 214303.
(59) Zevalkink, A.; et al. A practical field guide to thermoelectrics: Fundamentals, synthesis, and characterization. *Appl. Phys. Rev.* **2018**, *5*, 021303.